Structure and phase transitions in A-site ordered RBaMn$_2$O$_6$ (R = Pr, Nd) perovskites with a polar ground state

J. Blasco [1,*] G. Subías [1] M. L. Sanjuán [1] J. L. García-Muñoz [2] F. Fauth [3] and J. García[1]

[1]*Instituto de Nanociencia y Materiales de Aragón (INMA), CSIC-Universidad de Zaragoza, 50009 Zaragoza, Spain*
and Departamento de Física de la Materia Condensada, Universidad de Zaragoza, C/ Pedro Cerbuna 12, 50009 Zaragoza, Spain
[2]*Institut de Ciència de Materials de Barcelona, ICMAB-CSIC, Campus UAB, 08193, Bellaterra, Spain*
[3]*CELLS-ALBA Synchrotron Light Source, 08290 Cerdanyola del Vallès, Barcelona, Spain*

We report here a structural study of RBaMn$_2$O$_6$ (R = La, Pr, and Nd) compounds by means of synchrotron radiation x-ray powder diffraction and Raman spectroscopy. The three compounds are A-site ordered perovskites adopting the prototypical tetragonal structure at high temperature. A ferromagnetic transition is observed in the LaBaMn$_2$O$_6$ sample and the lattice parameters undergo anisotropic changes at T_C related to the orientation of the magnetic moments. Both PrBaMn$_2$O$_6$ and NdBaMn$_2$O$_6$ have a structural transition coupled to an electronic localization and an antiferromagnetic transition. In both cases, the x-ray diffraction patterns reveal that the low-temperature phase is orthorhombic with lattice parameters $a + b$, $b − a$, and c with respect to the tetragonal phase. Two possible solutions belonging to the space groups $Pmam$ and $P2_1am$ can yield accurate refinements of the x-ray patterns. However, the active modes in the low-temperature phase disclosed by the Raman spectroscopy clearly point to the noncentrosymmetric space group, $P2_1am$. The symmetry analysis of this transition unveils that the primary modes belong to the irreducible representations M5− and GM5− and the main distortions correspond to rotations of the MnO$_6$ octahedra and an asymmetric combination of stretching and scissoring modes of the basal oxygens in these octahedra. We conclude that the low-temperature phase is polar and the main contribution comes from the displacement of oxygen atoms from their centrosymmetric positions. However, negligible contribution from the asymmetric stretching associated with a Jahn-Teller distortion is found in this structural transition, suggesting the lack of ferroic orbital ordering of e_g ($3d_{x^2−y^2}$) orbitals in the orthorhombic ab plane. There is only one inequivalent site for the Mn atom in the low-temperature polar phase so charge ordering cannot account for the electronic localization having a structural origin.

I. INTRODUCTION

The physical properties of perovskite manganites have been widely studied in the last decades. These properties include colossal magnetoresistance, metal-insulator transitions, charge ordering (CO) transitions, orbital ordering (OO) transitions, and giant magnetocaloric effect among others. This variety of fascinating properties is due to the interplay between electronic, charge, magnetic, and orbital degrees of freedom [1–3]. These competitive forces manifest themselves especially in half-doped manganites [4]. At first, it was thought that large cations located in the A site of the perovskite structure (rare earth and divalent atoms) were limited to stabilizing both the crystal structure and the hole doping of the Mn sublattice. However, recent studies have revealed that the laminar ordering of A atoms strongly affects the physical properties of half-doped manganites [5]. It seems clear that these differences in the physical properties of compounds with

the same chemical composition but with different ordering degree of the A sublattice are strongly related to differences in the crystallographic structure that are not yet well understood. A prototype example of half-doped manganite with a simple perovskite structure where there is a solid solution between the rare earth atoms and the divalent dopant in the perovskite A site is Nd$_{0.5}$Sr$_{0.5}$MnO$_3$. This sample undergoes two successive magnetic transitions [6,7]. It develops a ferromagnetic (FM) order at $T_C \approx 280$ K and then a spin reorientation to yield an antiferromagnetic (AFM) order at $T_N \approx 160$ K. The latter transition is accompanied by a metal-insulator transition and a sudden change of the lattice parameters which consists of a strong shrinkage of the c axis while a and b axes expand [6]. The AFM structure is *CE*-type consisting of FM zigzag chains in the ab planes that are AFM coupled to each other and along the c axis [6]. This magnetic order is coupled to other arrangements: a charge ordering (CO) between Mn^{3+} and Mn^{4+} ions and an orbital ordering (OO) between two configurations of e_g ($3d_{z^2}$) orbitals of Mn^{3+} cations. This arrangement is common to other half-doped manganites that present the same kind of CO transition such as La$_{0.5}$Ca$_{0.5}$MnO$_3$, Pr$_{0.5}$Ca$_{0.5}$MnO$_3$, or Pr$_{0.5}$Sr$_{0.5}$MnO$_3$ [8–10]. The crystal structure of the ordered phase was refined in a monoclinic cell with the $P2_1/m$ space group (SG) and two

nonequivalent Mn sites [11]. However, both crystallographic refinements and spectroscopic measurements have determined that the CO between the two nonequivalent Mn atoms is only about 20%–25% of the maximum theoretical separation of one charge unit [11–13].

Amazingly, small changes in the hole doping lead to a different magnetic order in $Nd_{1-x}Sr_xMnO_3$ $(0.51 < x \leqslant 0.60)$ compounds [6]. These samples exhibit similar metal-insulator transition coupled to similar changes in the lattice parameters but they undergo a single magnetic transition to A-type AFM structure formed by FM layers that are AFM coupled each other along the c axis. This magnetic ground state was explained on the basis of a homogeneous ferroic OO of e_g $(3d_{x^2-y^2})$ orbitals in the ab planes. In this way, A-type structure arises from the AFM superexchange between the localized t_{2g} spins along the c axis and the FM double exchange between e_g $(3d_{x^2-y^2})$ spins in the ab plane. This model also implies a strong anisotropy in the transport properties with an insulating gap along the c axis and metallic behavior in the ab plane [14,15].

Different properties are observed in compounds where A atoms are not randomly distributed. This happens in $RBaMn_2O_6$ (R = rare earth atom or Y) where R and Ba are ordered in alternating [0 0 1] perovskite layers. This makes the MnO_2 sublattice sandwiched between the RO and BaO sublattices of very different sizes [5,16]. Accordingly, asymmetric distortions are forced in the MnO_6 octahedron. Regarding the physical properties, significant differences are observed depending on the R size. For compounds with smaller R atoms (R = Sm-Ho) or Y, the CO transition temperature is raised well above room temperature and different transitions and OO are reported depending on the R atom [17–20]. However, for light R atoms (La, Pr, Nd), the FM correlations are enhanced with respect to the parent simple perovskites [5,16,21]. On cooling, the FM transition is followed by a spin reorientation in Pr- and Nd-based compounds transforming to an A-type AFM structure. Preliminary studies on these compounds reported that the crystal structure remains tetragonal with no CO or OO transitions at any temperature [16]. However, neutron powder diffraction experiments [22] outlined a more complicated scenario and a fractional transition from the FM to AFM (CE-type, instead of A-type) phase was observed in $LaBaMn_2O_6$. Likewise, the coexistence of a minority fraction of CE-type and majority A-type phases is noticed in the ground state of $PrBaMn_2O_6$ whereas a pure A-type phase is present for $NdBaMn_2O_6$.

It was thought that $RBaMn_2O_6$ (R = Pr, Nd) has no tilts of MnO_6 octahedra but a recent study of single-crystal x-ray diffraction detected two successive transitions in $NdBaMn_2O_6$ which imply the rotations of these octahedra [23]. The authors concluded that the ground state of this sample is a noncentrosymmetric SG, $P2_1am$, and a spontaneous electric polarization along the a axis is predicted. The authors also concluded that the metal-insulator transition is coupled to an OO transition at 290 K without the concomitant CO observed in related simple perovskites. However, the magnetic transition temperature is lowered down to 235 K on the basis of the temperature dependence of the anisotropic magnetic susceptibility curves. In this way, spectroscopic ellipsometry and Raman scattering spectroscopy also detected anomalies asso-

ciated with the electric and magnetic transitions at 290 and 235 K, respectively [24]. Significant charge transfer between O $2p$ and Mn $3d$ states was also found. Such a low value of T_N is at odds with previous neutron powder diffraction studies where the long-range AFM order was observed in the range 275–290 K [22,25]. In a later study the same authors, using a larger crystal, identified a series of superstructure peaks that were not compatible with the structure previously proposed and concluded that the $NdBaMn_2O_6$ is isostructural with $SmBaMn_2O_6$ and not compatible with an A-type magnetic ordering [26]. Therefore, the crystallographic and magnetic structures of $NdBaMn_2O_6$ are now an open question. The same can be said for $PrBaMn_2O_6$ which has similar properties [22,27] and whose crystal structure at low temperature has not been deeply studied. A cause might be that the study of the structural properties of these compounds using single-crystal diffraction is a challenging task due to the occurrence of strong twinning, multiple scattering, and self-absorption problems. These difficulties are less relevant in powder diffraction and these obstacles can be overcome using synchrotron x-ray powder diffraction (SXRPD) measurements with higher angular resolution and flux than conventional diffractometers.

In this work we report a structural study of $NdBaMn_2O_6$ and $PrBaMn_2O_6$ using SXRPD between 100 and 400 K. Our study has revealed that both compounds are isostructural in the two limit temperatures but a different sequence of phase transitions is found at intermediate temperatures. The study is completed with a symmetry analysis and Raman spectroscopy in order to identify the condensed modes that account for the phase transitions and elucidate the presence or absence of a symmetry center at low temperature.

II. EXPERIMENTAL SECTION

Single crystals of $PrBaMn_2O_6$ and $NdBaMn_2O_6$ were grown using the floating zone method from polycrystalline precursors. Stoichiometric amounts of dried Pr_6O_{11} (or Nd_2O_3), $BaCO_3$, and Mn_2O_3 were mixed, ground, and heated at 1000 °C overnight. The resulting powder is reground, pressed into pellets, and sintered at 1250 °C in a gas flow of H_2/Ar mixture (2% H_2) saturated in water vapor to achieve a reductive atmosphere ($P_{O2} \approx 10^{-11}$ bars). This is required to prevent the formation of $BaMnO_3$ impurity [21]. Then, the pellets are reground, pressed into rods, and sintered at 1375 °C for 24 h in the same atmosphere. This procedure was also used to obtain polycrystalline $LaBaMn_2O_6$ from dried La_2O_3. The rods were mounted in a homemade floating zone (FZ) furnace with two semielliptical mirrors [28]. The growth was carried out in the same reductive atmosphere with an overpressure of 2 bars. The seed and feed bars with diameters of 3.5 mm rotated in opposite directions at 20 rpm with a growth speed of 6 mm/h and the total lengths of the growth were 50 and 52 mm for Pr- and Nd-based samples, respectively. Some parts of the boules spontaneously split, leaving bright faces corresponding to the $(0, 0, 1)_t$ plane.

After this step, the obtained products are oxygen deficient $RBaMn_2O_{5+\delta}$ (R = La, Pr, Nd), with $\delta \approx 0.1$. The next step consists of topotactic oxidation by heating the boules (or sintered rod for polycrystalline samples) at 400 °C–450 °C in an oxygen current flow for 24 h yielding the stoichiomet-

ric $RBaMn_2O_6$ compounds. Some parts of the boules were ground and analyzed by powder x-ray-diffraction. Rietveld analysis of the x-ray patterns using the FULLPROF package program [29] indicated that the crystals were single phase without detectable impurities. The chemical composition of the powders was also tested using the wavelength dispersive x-ray fluorescence spectrometry (Advant'XP+ model from Thermo-ARL) and the R:Ba:Mn stoichiometry agreed with the expected values within the experimental error (1%).

SXRPD patterns were measured at the MSPD beamline [30] of the ALBA synchrotron (Cerdanyola del Vallès, Spain) using high-throughput position sensitive detector MYTHEN. Both the high photon flux of the beamline and the good signal to noise sensitivity of the detector allows detecting minor superstructure peaks. The samples were loaded in a borosilicate glass capillary (diameter of 0.5 mm) and kept spinning during data acquisition. A short wavelength, $\lambda = 0.4128$ Å, was selected to reduce absorption. The value of λ was calibrated using a NIST standard silicon. We have performed two types of measurements; standard patterns to refine unit cells were collected in heating and cooling ramps between 100 and 440 K. The rate was 0.5 K min^{-1} and the total acquisition time was 6 min. With this procedure, we collected a pattern every 3 K on average. Secondly, SXRPD patterns with very good statistics were measured at selected temperatures for each sample with a total acquisition time of 30 min/pattern to perform a full structural characterization.

Magnetic measurements were carried out with a commercial Quantum Design (SQUID) magnetometer. The dc magnetization was measured between 5 and 400 K with an external field ranging between 0.5 and 1 kOe. Electrical dc resistivity measurements were made between 10 and 350 K on rectangular bars cut from polycrystalline pellets with a typical size of $2 \times 2 \times 9$ mm^3. A Quantum Design physical property measurement system (PPMS) was utilized for this purpose. The conventional four-probe configuration was employed, and electrodes were made using silver paint. Differential scanning calorimetry (DSC) was measured by using a DSC 2910 from TA instruments with samples sealed in aluminum pans.

Raman spectra of single-crystalline samples were recorded in a DILOR XY spectrometer equipped with a liquid-nitrogen cooled CCD detector. The 496.5 and 514.5 nm lines of an Ar$^+$-ion laser and the 647.1 nm line of a Kr$^+$ laser were used as excitation sources. An ULWD $50\times$ microscope objective lens of an Olympus BH-2 microscope was used both for excitation and dispersed light collection. Variable-temperature measurements were performed from 77 to 295 K using an Air-Liquide cryostat and liquid-nitrogen refrigeration.

III. RESULTS AND DISCUSSION

A. LaBaMn$_2$O$_6$

LaBaMn$_2$O$_6$ is a prototype of A-site ordered perovskite. It adopts the tetragonal structure without MnO$_6$ tilts and SG $P4/mmm$ [21]. It undergoes a magnetic transition as can be seen in the $M(T)$ curves in Fig. 1. The transition is typical of a FM ordering whose onset occurs at 356 K with a $T_C = 329$ K taken at the inflection point. SXRPD patterns were collected between 150 and 440 K for this sample and the tetragonal
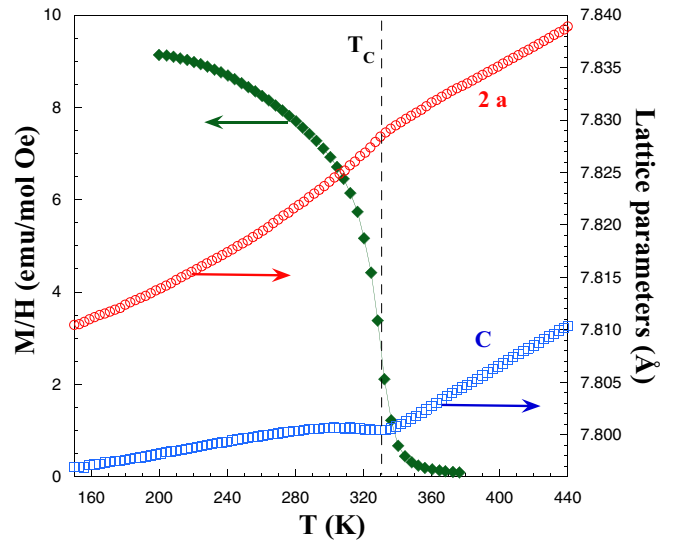

FIG. 1. Temperature dependence of the magnetization and the lattice parameters for LaBaMn$_2$O$_6$. The a axis has been multiplied by 2 for the sake of comparison.

symmetry is preserved in the whole temperature range. The only notable anomaly is the sudden change observed in the lattice parameters at T_C (see Fig. 1). The a axis shows a small downturn at T_C while the anomaly is more abrupt in the c axis with a local minimum at T_C and then an expansion of this axis just below T_C. These changes are clearly related to the magnetic arrangement of LaBaMn$_2$O$_6$ where the Mn moments are oriented along the c axis [22] producing a small expansion of this axis. The refined structural parameters at three selected temperatures (150, 295, and 440 K) are given in Table I and the observed and calculated patterns of the SXRPD Rietveld profiles are shown in Fig. S1 in the Supplemental Material [31].

B. PrBaMn$_2$O$_6$

Figure 2 shows the temperature dependence of the magnetization and electrical resistivity for PrBaMn$_2$O$_6$. Two magnetic transitions can be observed in the temperature range between 5 and 400 K with a remarkable hysteresis. Focusing on the cooling curve, the sample is clearly paramagnetic (PM) above 330 K. Below this temperature, there is a pronounced increase of the magnetization signal characteristic of a FM order with a $T_C = 309$ K. Further cooling the sample, an abrupt drop in the magnetization is noticeable below 245 K and the second transition takes place at $T_N = 235$ K indicating a long AFM order. Both transition temperatures have been taken at their respective inflection points of the $M(T)$ curve. In the warming curve, T_N goes up to 260 K whereas T_C remains unchanged. The AFM transition is coupled to a jump of the electrical resistivity and both features are characterized by a significant temperature hysteresis between the measurements made on heating and on cooling. The hysteresis agrees with a first-order transition. All these properties match those previously reported for similar compounds [16,22].

Regarding the structural properties of PrBaMn$_2$O$_6$, the SXRPD pattern measured at the highest temperatures

TABLE I. Structural parameters of LaBaMn$_2$O$_6$ obtained from the Rietveld analysis at the indicated temperatures. The space group for all temperatures is $P4/mmm$.

	Atom	x	y	z	$B_{iso}(\text{Å}^2)$
$T = 440$ K					
$a = 3.91946(1)$ Å	La	0	0	0	0.83(4)
$c = 7.81037(2)$ Å	Ba	0	0	$\frac{1}{2}$	0.55(4)
$V = 119.369(1)$ Å^3	Mn	$\frac{1}{2}$	$\frac{1}{2}$	0.24933(44)	0.47(1)
$R_p(\%) = 4.95$	O1	$\frac{1}{2}$	$\frac{1}{2}$	0	2.42(44)
$R_{wp}(\%) = 7.13$	O2	$\frac{1}{2}$	0	0.23372(62)	1.27(7)
$R_{Bragg}(\%) = 2.5$	O3	$\frac{1}{2}$	$\frac{1}{2}$	$\frac{1}{2}$	0.79 (22)
$\chi^2 = 2.95$					
$T = 295$ K					
$a = 3.91189(1)$ Å	La	0	0	0	0.65(4)
$c = 7.80047(2)$ Å	Ba	0	0	$\frac{1}{2}$	0.40(4)
$V = 120.005(1)$ Å^3	Mn	$\frac{1}{2}$	$\frac{1}{2}$	0.24872(49)	0.35(1)
$R_p(\%) = 4.75$	O1	$\frac{1}{2}$	$\frac{1}{2}$	0	1.13(51)
$R_{wp}(\%) = 6.65$	O2	$\frac{1}{2}$	0	0.23625(67)	0.99(7)
$R_{Bragg}(\%) = 2.2$	O3	$\frac{1}{2}$	$\frac{1}{2}$	$\frac{1}{2}$	0.46(40)
$\chi^2 = 4.2$					
$T = 150$ K					
$a = 3.90560(1)$ Å	La	0	0	0	0.49(2)
$c = 7.79766(3)$ Å	Ba	0	0	$\frac{1}{2}$	0.15(2)
$V = 118.943(1)$ Å^3	Mn	$\frac{1}{2}$	$\frac{1}{2}$	0.25063(36)	0.25(8)
$R_p = 4.93$	O1	$\frac{1}{2}$	$\frac{1}{2}$	0	0.35(24)
$R_{wp} = 7.20$	O2	$\frac{1}{2}$	0	0.23138(51)	0.84(9)
$R_{Bragg} = 2.4$	O3	$\frac{1}{2}$	$\frac{1}{2}$	$\frac{1}{2}$	0.33(25)
$\chi^2 = 6.2$					

(440 K) exhibits a tetragonal cell with no MnO$_6$ octahedra tilts isostructural to LaBaMn$_2$O$_6$. The comparison between the patterns collected at 400 and 100 K shows clear differences [see Supplemental Material [31]]. These can be classified into two types: the splitting of a good number of main peaks and
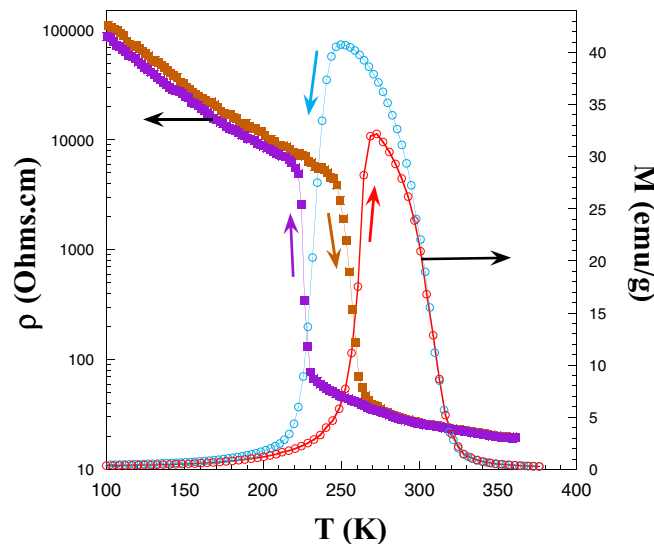

FIG. 2. Resistivity and magnetization of PrBaMn$_2$O$_6$ as a function of temperature in cooling and heating runs indicated by arrows. The applied magnetic field in the magnetic measurement was 1 kOe.

the appearance of superstructure peaks indexed as $(\frac{h}{2}, \frac{k}{2}, l)_t$ in the 100 K pattern, where the subscript t refers to the high-temperature tetragonal cell (Fig. S3) [31]. On heating, these superstructure peaks vanish at T_N, suggesting a structural phase transition coupled to the magnetic one and a nontetragonal unit cell below T_N. In order to determine the structure of this compound at low temperature, we have applied the symmetry adapted mode description of distorted structures using the tool ISODISTORT [32]. The high-temperature tetragonal phase is considered as the parent structure and we have identified the irreducible representation (Irrep) M5−, $k = (\frac{1}{2}, \frac{1}{2}, 0)$, with respect to $P4/mmm$ as associated with the rotation of MnO$_6$ octahedra. In order to further limit the search, we have taken advantage of the results obtained by neutron diffraction that have shown that the magnetic ground state of this compound is an A-type AFM ordering. We have identified this ordering with the magnetic Irrep mGM5−, $k = (0, 0, 0)$. In this way, the possible distorted structures that present MnO$_6$ rotations compatible with the reported magnetic structure are $Pmma$ (orthorhombic and centrosymmetric), $Pmc2_1$ (orthorhombic and noncentrosymmetric), and $P2_1/m$ (monoclinic and centrosymmetric). The latter can be discarded as no evidence of monoclinic distortion has been found in our SXRPD patterns. The refinements with the two orthorhombic models give results with similar goodness factors. In fact, the occurrence of both cells was deduced from a previous symmetry analysis and the main difference concerns the type of MnO$_6$ octahedra tilting [33]. According to the symmetry
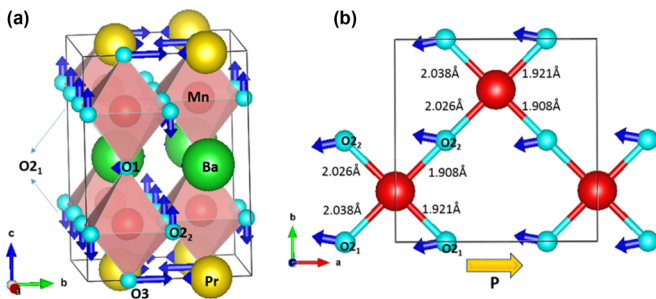
FIG. 3. (a) Crystal structure of $PrBaMn_2O_6$ with the oxygen shifts produced by the modes belonging to the Irrep M5−. (b) Detail of the base of the MnO_6 octahedron with bond lengths and the displacements due to the modes belonging to Irrep GM5− and the expected polarization direction.

analysis, the transition from $P4/mmm$ into $Pmma$ is expected to be continuous while the transition into $Pmc2_1$ should be of first order in agreement with the hysteresis in its physical properties (see Fig. 2). However, the definitive answer is given by the Raman spectroscopy as can be seen later. The spectra disclose that the number of observed modes at low temperature is only compatible with the noncentrosymmetric structure. Therefore, we have refined the low SXRPD pattern using the SG $P2_1am$ (a setting of $Pmc2_1$ by exchanging a and c axes). The relationship for the lattice parameters between the parent and the distorted phases is $a_o \approx \sqrt{2}a_t$, $b_o \approx \sqrt{2}a_t$, and $c_o \approx c_t$. It is worth emphasizing that this structure is similar to that published for $NdBaMn_2O_6$ in a study by Yamada *et al.* [23]. We have performed the mode decomposition to relate parent and distorted phases. There are 17 active modes belonging to 5 Irreps: GM1+, GM5−, M2+, M3+, and M5−. The primary modes belong to Irreps GM5− and M5− with global amplitude values of 0.42(4) and 0.36(2) Å, respectively. The contributions of modes belonging to M2+ and M3+ are negligible and those from GM1+ are much smaller. It should be noted here that the distortion associated with the Irrep M3+ corresponds to a Jahn-Teller distortion of the basal oxygens and the refinement yields a null contribution of it. Figure 3 shows the main modes involved in the structural transition. The oxygen shifts associated with the Irrep M5− correspond to a corner-linked tilting of the MnO_6 octahedra in agreement with the two-tilt system $a^-a^-c^0$ following Glazer's terminology [34]. It is composed of three individual modes. The basal oxygens have opposite shifts along the c axis as indicated in Fig 3(a). These movements are coupled and they have point symmetry A_1. On the other hand, the apical oxygens also have opposite shifts along the b axis (point symmetry B_u) but they are not coupled and, in fact, the displacement of O1 is significantly smaller than that of O3, probably due to the steric effect produced by the large size of the Ba^{2+} cation. This makes the MnO_6 octahedron no longer regular when rotating. It is noteworthy that the distortion belonging to the Irrep M2+ implies the tilt $a^0a^0c^+$ and although its amplitude is practically zero in this case, the rotational distortion of MnO_6 octahedra in this SG belongs to the three-tilt system $a^-a^-c^+$ as indicated in Ref. [33]. Regarding the displacements ascribed to Irrep GM5−, the most significant are shown in Fig. 3(b) and concern the basal oxygens. They are composed by an asymmetric stretching mode (point

symmetry B_1) and an asymmetric scissoring mode (B_2). The result is two short and two long Mn-O2 distances resulting in a trapezoid shape for the base of the MnO_6 octahedra. Another two modes of the Irrep GM5− with significant amplitude (B_u) are acting on the two apical oxygens with shift along the b axis. However, the amplitude of the GM5− modes acting on the cations is negligible. The bond lengths between Mn atoms and apical oxygens are Mn-O1 = 1.931(3) Å and Mn-O3 = 1.901(4) Å. Accordingly, the octahedral coordination of Mn is composed of four short distances (around 1.92 Å) and two long ones (about 2.02 Å) but the geometric arrangement has nothing to do with a Jahn-Teller distortion so that the ferroic OO of $3d_{x^2-y^2}$ e_g orbitals in this compound at low temperature is very unlikely. On the other hand, the approximation of two basal oxygens to the Mn atom suggests an increase in the covalence of these bonds in agreement with previous spectroscopic studies on a related compound [24]. The refined structural parameters are summarized in Table II and the fits are shown in Fig. S2 [31].

Focusing on the structural transition, this is associated with strong splitting of many diffraction peaks as can be seen in the example of Fig. 4(a). Moreover, there is a wide temperature range where the high- and low-temperature phases coexist. We have performed Rietveld analysis quantifying the phase ratio in this temperature range in the heating and cooling runs and the results are collected in Fig. 4(b). We have observed a temperature hysteresis similar to the one observed in the macroscopic properties [compare Figs. 2 and 4(b)]. Another interesting feature is the phase transformation. It is complete in the heating run indicating that the orthorhombic phase is fully transformed into the tetragonal one at 275 K. However, the diffraction peaks from the high-temperature phase get smaller and wider on cooling but at low temperature, they transform into diffuse scattering hard to quantify. This diffuse contribution is still noticeable at 100 K [see Fig. S4 in the Supplemental Material [31]] and suggests the occurrence of nanoscopic regions of the high-temperature phase at this temperature. This fact could account for the metamagnetic transitions reported [35] for this compound as an external magnetic field would favor the stability of the ferromagnetic high-temperature phase.

Figure 5 shows the evolution of the structural parameters as a function of the temperature obtained under heating conditions. The strong changes can be seen by comparing the equivalent axes in the two phases. Thus, the tetragonal a axis undergoes a strong expansion at around T_N. The orthorhombic distortion is clear just below the transition temperature but it decreases on cooling to give a pseudotetragonal phase at 100 K. The opposite trend is observed in the c axis with a strong shrinkage at the phase transition. These features are typical of CO transition in manganites without layered ordering but this scenario can be discarded for the present compound as there is a unique site for Mn atoms in the low-temperature phase. If we look at the evolution of the unit cell volume on cooling, a sharp expansion is noticeable at the transition indicating that the volume of the orthorhombic phase is greater than the tetragonal one. This is in accordance with the virial theorem for metal-insulator transitions where an electron localization is accompanied by an expansion of the unit cell volume because changes in the kinetic and potential

TABLE II. Structural parameters of $PrBaMn_2O_6$ obtained from the Rietveld analysis at the indicated temperatures.

	Atom	x	y	z	$B_{iso}(\text{Å}^2)$
$T = 440$ K ($P4/mmm$)	Pr	0	0	0	1.07(4)
$a = 3.90856(1)$ Å	Ba	0	0	$\frac{1}{2}$	0.68(4)
$c = 7.76706(2)$ Å	Mn	$\frac{1}{2}$	$\frac{1}{2}$	0.24880(31)	0.58(1)
$V = 118.656(1)$ Å^3	O1	$\frac{1}{2}$	$\frac{1}{2}$	0	2.42(35)
$R_p(\%) = 4.7$	O2	$\frac{1}{2}$	0	0.22947(45)	1.48(6)
$R_{wp}(\%) = 6.8$	O3	$\frac{1}{2}$	$\frac{1}{2}$	$\frac{1}{2}$	0.71(21)
$R_{Bragg}(\%) = 2.1$					
$\chi^2 = 5.4$					
$T = 330$ K ($P4/mmm$)	Pr	0	0	0	0.90(3)
$a = 3.90442(1)$ Å	Ba	0	0	$\frac{1}{2}$	0.58(2)
$c = 7.75327(3)$ Å	Mn	$\frac{1}{2}$	$\frac{1}{2}$	0.24882(29)	0.51(1)
$V = 118.194(1)$ Å^3	O1	$\frac{1}{2}$	$\frac{1}{2}$	0	2.09(30)
$R_p(\%) = 4.6$	O2	$\frac{1}{2}$	0	0.23015(42)	1.13(5)
$R_{wp}(\%) = 6.8$	O3	$\frac{1}{2}$	$\frac{1}{2}$	$\frac{1}{2}$	0.52(13)
$R_{Bragg}(\%) = 2.25$					
$\chi^2 = 5.4$					
$T = 100$ K ($P2_1am$)					
$a = 5.55775(3)$ Å	Pr	0.000	0.7435(3)	0	0.34(2)
$b = 5.55462(3)$ Å	Ba	0.000	0.7487(4)	$\frac{1}{2}$	0.41(3)
$c = 7.62299(1)$ Å	Mn	0.000	0.2500	0.2471(2)	0.31(1)
$V = 235.331(2)$ Å^3	O1	$-0.035(6)$	0.281(4)	0	0.21(19)
$R_p(\%) = 4.3$	O2$_1$	0.732(2)	0.003(2)	0.7827(10)	0.28(13)
$R_{wp}(\%) = 5.8$	O2$_2$	0.232(2)	0.503(2)	0.7594(10)	0.31(13)
$R_{Bragg}(\%) = 1.61$	O3	$-0.018(8)$	0.233(7)	$\frac{1}{2}$	0.52(13)
$\chi^2 = 4.3$					

energies across a first-order transition are opposite in sign [36]. When comparing the refined data for the high- and low-temperature phases, the changes are minimal in the average Mn-O ($\langle$Mn-O$\rangle$) distance being 1.954 Å for the data refined at 440 and 100 K. However, the temperature dependence of $\langle$Mn-O$\rangle$ also shows an anomaly at the phase transition temperature

as can be seen in Fig. 5(d). This average distance decreases in the high-temperature phase mirroring the evolution of the unit cell volume and exhibits an abrupt jump at T_N that compensates the previous decrease. Below T_N, $\langle$Mn-O$\rangle$ remains almost constant. Another significant difference concerns the distribution of the Mn-O bond lengths in the ab plane. There
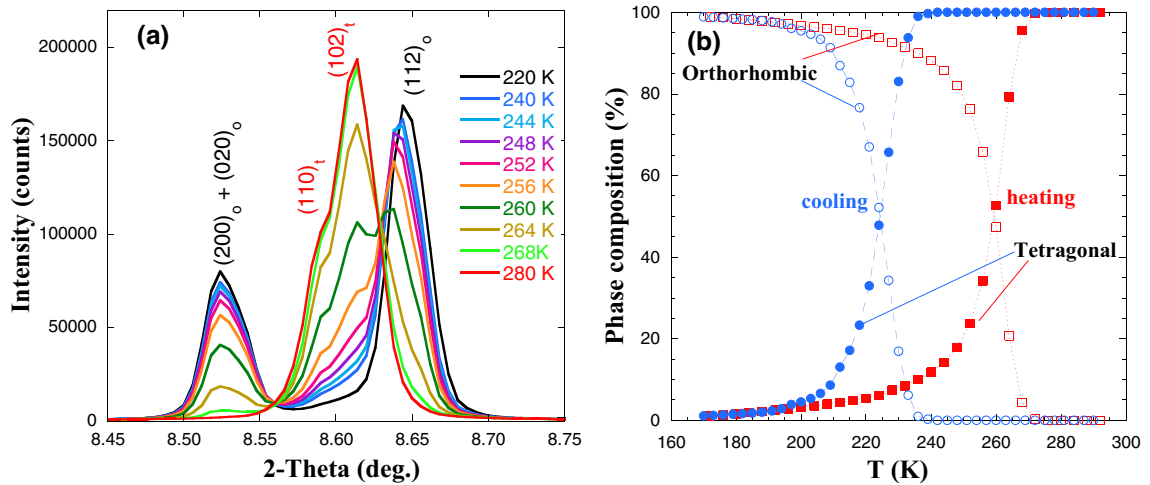

FIG. 4. (a) Comparison of a region of SXRPD pattern collected at selected temperatures after heating from 100 K for $PrBaMn_2O_6$. Subscripts in the index refer to orthorhombic (*o*) and tetragonal (*t*) cells. (b) Quantification of the orthorhombic (open symbols) and tetragonal (closed symbols) phases obtained from the Rietveld analysis of the SXRPD patterns when heating from 100 K (red squares) and cooling from 440 K (blue circles).
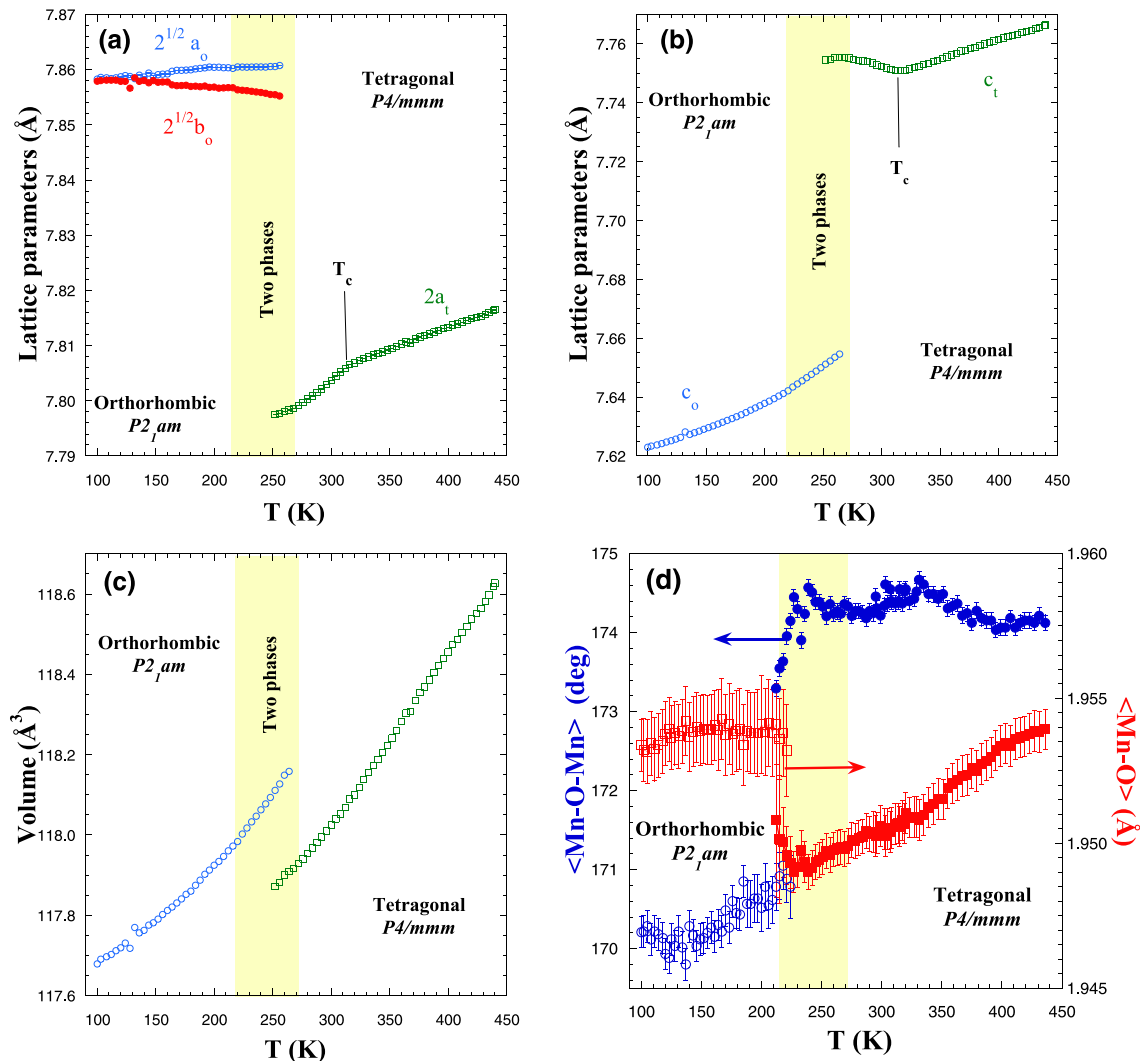
FIG. 5. Temperature dependence of the lattice parameters for $PrBaMn_2O_6$ in the heating ramp: (a) *a* and *b* axes, (b) *c* axis, and (c) unit cell volume. The parameters of the *ab* plane have been multiplied by 2 (tetragonal case) and $\sqrt{2}$ (orthorhombic case) for the sake of comparison. (d) Temperature dependence of the average Mn-O-Mn bond angle (circles) and Mn-O lattice distance (squares) in the cooling ramp.

is a single Mn-O2 distance in the tetragonal phase which becomes a mixture of two long and two short distances in the low-temperature phase as indicated in Fig. 3(b). A more important change is observed in the evolution of the average ⟨Mn-O-Mn⟩ bond angle. It reaches a value of 174.1 ° at 440 K and only 169.8 ° at 100 K. Figure 5(d) shows that the change is abrupt at the temperature where electronic localization occurs [compare Figs. 2 and 5(d)]. The decrease of ⟨Mn-O-Mn⟩ produces a narrowing of the electronic bandwidth and opens a gap at the Fermi energy. However, the low-temperature phase only has a single nonequivalent site for Mn atoms so electronic localization cannot lead to a CO. Instead, our results suggest that this system is metalliclike for small distortions but a periodic distortion alternating long and short Mn-O bonds in the *ab* plane opens a gap at the Fermi energy in the low-temperature phase. In this way, it could be considered as a type of effective charge density wave centered on the Mn-O bonds without charge transfer between neighboring MnO_6 octahedra. A similar mechanism was proposed for metal-insulator transitions in related nickelates associated with a breathing distortion [37].

In the present case, the electronic localization is coupled to the asymmetric stretching of the MnO_6 octahedra.

Damped by the large structural modifications observed at T_N, it is difficult to appreciate the small changes observed at T_C. As in the FM transition of $LaBaMn_2O_6$, a small contraction of the *a* axis coupled to a small expansion of the *c* axis can be seen at T_C in Figs. 5(a) and 5(b). This indicates that both compounds, $LaBaMn_2O_6$ and $PrBaMn_2O_6$, have a similar FM transition with the magnetic moments oriented along the same direction (*c* axis).

C. NdBaMn$_2$O$_6$

Figure 6 compares the temperature dependence of the magnetization and electrical resistivity in $NdBaMn_2O_6$. We find many similarities with the properties reported in $PrBaMn_2O_6$. In this way, we observe a similar jump of the electrical resistivity with a significant temperature hysteresis between the heating and cooling runs. Regarding the magnetic properties, we find some difference since in this case two magnetic
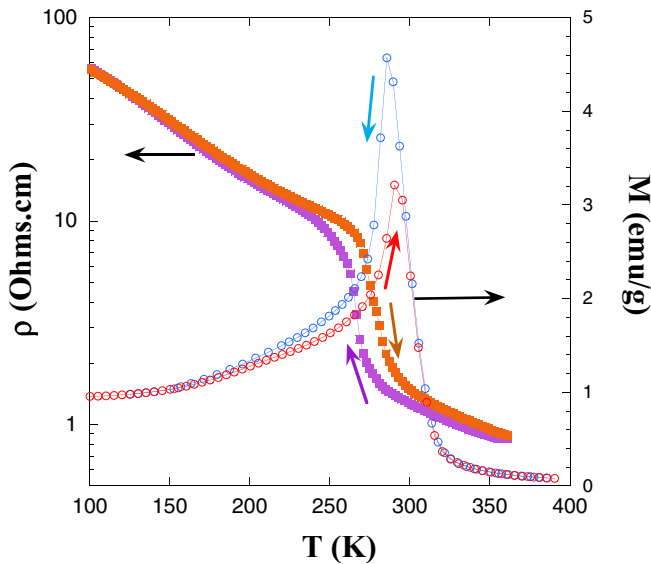
FIG. 6. Resistivity and magnetization of NdBaMn$_2$O$_6$ as a function of temperature in cooling and heating runs indicated by arrows. The applied magnetic field in the magnetic measurement was 500 Oe.

transitions are not so clearly evidenced. The magnetization curves in Fig. 6 exhibit a sharp peak in accordance with previous reports [22,23,25]. The magnetization curves obtained from cooling or heating measurements present a wide range of irreversibility between 297 and 200 K which coincides with the hysteresis observed in the electrical properties of the same sample. The peak is achieved at 292 K when the sample is heated from 5 K while it is at 287 K on cooling from 350 K. The shape of the magnetization curve can be explained by referring to a previous neutron diffraction study indicating that NdBaMn$_2$O$_6$ develops an *A*-type AFM ordering [22]. This accounts for the sharp decrease of the magnetization below the peak temperature. From the inflection point of the *M(T)* curve, one can infer the value of $T_N = 287$ K in the heating run (281 K in the cooling run). Above this magnetic transition, FM correlations are present in this compound producing an increase in the magnetization. However, neutron diffraction revealed that long-range FM ordering is not completely established in this compound but occurrence of short-range correlations is clearly evidenced [25]. This is the fundamental difference with respect to the PrBaMn$_2$O$_6$ case where a long-range FM order was established in a short temperature range.

Concerning the structural properties of NdBaMn$_2$O$_6$, we have measurements with very good statistics at four selected temperatures: 100, 295, 320, and 440 K. At 440 K, NdBaMn$_2$O$_6$ is isostructural to the two previous samples with the same tetragonal structure. At 100 K, the pattern shows features similar to the ones observed in PrBaMn$_2$O$_6$, that is, the splitting of some fundamental diffraction peaks and the occurrence of similar $(\frac{h}{2}, \frac{k}{2}, l)_t$ superstructure peaks (see Fig. S7 in the Supplemental Material [31]). This suggests that PrBaMn$_2$O$_6$ and NdBaMn$_2$O$_6$ are isostructural at low temperature. According to Ref. [26], NdBaMn$_2$O$_6$ could be isostructural to SmBaMn$_2$O$_6$. Our study does not support this statement. We did not find $(\frac{h}{4}, \frac{k}{4}, l)_t$ superstructure peaks in

the SRXPD patterns at 100 K with a resolution limit for the intensity of five orders of magnitude related to the fundamental reflections. This limit is sufficient to detect the superstructure peaks of SmBaMn$_2$O$_6$ [38]. Reference [26] suggests that $(\frac{h}{4}, \frac{k}{4}, l)_t$ peaks are six orders of magnitude lower than the fundamental reflections. This would be below our resolution limit so we have explored this possibility. First of all, the refinement in the large cell isostructural to SmBaMn$_2$O$_6$ did not improve our previous refinements despite a greater number of free parameters. The $(\frac{h}{4}, \frac{k}{4}, l)_t$ peaks arise from distortion modes ascribed to the Irrep SM2 associated with the point $(\frac{1}{4}, \frac{1}{4}, 0)$ in the first Brillouin zone. Some of these modes give rise to two different environments for the Mn atoms. Our simulations have shown that mode amplitudes producing a charge segregation of only $0.06\,e^-$ between the two Mn atoms would be already visible in the SRXPD patterns. This result makes a CO transition in NdBaMn$_2$O$_6$ highly unlikely. Finally, the CO/OO structure of SmBaMn$_2$O$_6$ is not compatible with the *A*-type AFM ordering of the Mn atoms previously determined for PrBaMn$_2$O$_6$ and NdBaMn$_2$O$_6$ [22,25].

Therefore, we have utilized the same model used in the study of the PrBaMn$_2$O$_6$ sample to refine the SXRPD data at 100 K of the NdBaMn$_2$O$_6$ compound. In this case, equally good fits were obtained using both SGs: *Pmam* or *P2$_1$am*. As with PrBaMn$_2$O$_6$, Raman spectroscopy agrees with the second option. The refined parameters are summarized in Table III and the observed and calculated patterns of the SXRPD Rietveld profiles are displayed in Fig. S5 [31]. The set of condensed modes with respect to the parent structure are similar to those observed in the PrBaMn$_2$O$_6$ compound. Again the primary modes belong to Irreps GM5− and M5− with global amplitude values of 0.40(4) and 0.43(2) Å, respectively (see Table IV). We observe an increase in the amplitude of M5− modes indicating an increase in the rotation of MnO$_6$ octahedra. Modes of the Irrep GM1+ are secondary while modes of Irreps M2+ and M3+ are negligible. In this case, we have set the amplitude of the GM5− mode corresponding to the Ba atom to zero in order to fix the origin of the noncentrosymmetric structure and we notice small polar shifts of both Mn and Nd atoms which are added to the oxygen shifts already observed in the PrBaMn$_2$O$_6$ sample. Anyway, the main polar shifts correspond to oxygen atoms and are similar to the ones observed in PrBaMn$_2$O$_6$ (see Fig. 3). In this case the bond lengths between Mn atoms and apical oxygens are Mn-O1 = 1.919(2) Å and Mn-O3 = 1.911(4) Å. The basal Mn-O distances are 2.034(13), 2.040(13), 1.902(14), and 1.905(14) with a distribution similar to the one displayed in Fig. 3(b). The solution found here is similar to the one reported by Yamada *et al.* in Ref. [23]. However, these authors analyzed their structural data based on a Jahn-Teller type distortion mode analysis deducing a ferroic OO of $3d_{x^2-y^2}$ orbitals. In order to compare the results of both refinements, we have performed a mode decomposition of the structural parameters reported by Yamada *et al.* [23]. For this purpose we have used the AMPLIMODES program from the Bilbao Crystallographic server [39]. The comparison is summarized in Table IV. As can be seen, both refinements lead to similar mode decomposition. In this way, we observe similar amplitude for the main M5− modes and small amplitudes for modes of the Irreps GM1+, M2+, and M3+. In the case of the last two

TABLE III. Structural parameters of NdBaMn$_2$O$_6$ obtained from the Rietveld analysis at the indicated temperatures.

	Atom	x	y	z	B_{iso}($Å^2$)
$T = 440$ K ($P4/mmm$)	Nd	0	0	0	0.96(2)
$a = 3.90535(1)$ Å	Ba	0	0	$\frac{1}{2}$	0.61(2)
$c = 7.75177(2)$ Å	Mn	$\frac{1}{2}$	$\frac{1}{2}$	0.2477(3)	0.49(1)
$V = 118.228(1)$ Å^3	O1	$\frac{1}{2}$	$\frac{1}{2}$	0	2.11(19)
$R_p(\%) = 2.6$	O2	$\frac{1}{2}$	0	0.2311(2)	1.36(3)
$R_{wp}(\%) = 3.8$	O3	$\frac{1}{2}$	$\frac{1}{2}$	$\frac{1}{2}$	0.49(11)
$R_{Bragg}(\%) = 1.2$					
$\chi^2 = 3.8$					
$T = 320$ K($Cmmm$)	Nd	0.2502(3)	0	0	0.71(2)
$a = 7.80583(6)$ Å	Ba	0.2502(3)	0	$\frac{1}{2}$	0.48(2)
$b = 7.80280(7)$ Å	Mn	0	0.2496(3)	0.2470(2)	0.38(1)
$c = 7.73213(1)$ Å	O1	0	0.2759(13)	0	0.13(17)
$V = 470.943(6)$ Å^3	O2$_1$	0	0	0.2316(21)	0.76(35)
$R_p(\%) = 2.6$	O2$_2$	0	$\frac{1}{2}$	0.2522(17)	1.81(36)
$R_{wp}(\%) = 3.7$	O2$_3$	$\frac{1}{4}$	$\frac{1}{4}$	0.2227(9)	0.56(16)
$R_{Bragg}(\%) = 1.2$	O3	0	0.2559(21)	$\frac{1}{2}$	0.84(18)
$\chi^2 = 3.7$					
$T = 295$ K($Cmmm$)	Nd	0.2506(3)	0	0	0.66(2)
$a = 7.80949(3)$ Å	Ba	0.2499(3)	0	$\frac{1}{2}$	0.47(2)
$b = 7.79996(3)$ Å	Mn	0	0.2495(3)	0.2470(2)	0.36(1)
$c = 7.72405(1)$ Å	O1	0	0.2759(16)	0	0.39(18)
$V = 470.501(2)$ Å^3	O2$_1$	0	0	0.2260(16)	0.52(24)
$R_p(\%) = 2.5$	O2$_2$	0	$\frac{1}{2}$	0.2548(13)	1.42(25)
$R_{wp}(\%) = 3.5$	O2$_3$	$\frac{1}{4}$	$\frac{1}{4}$	0.2238(9)	0.79(11)
$R_{Bragg}(\%) = 1.1$	O3	0	0.2607(23)	$\frac{1}{2}$	0.71(17)
$\chi^2 = 3.4$					
$T = 100$ K ($P2_1am$)					
$a = 5.54805(3)$ Å	Nd	$-0.0050(6)$	0.7423(3)	0	0.47(2)
$b = 5.54447(4)$ Å	Ba	0.0000	0.7478(4)	$\frac{1}{2}$	0.12(2)
$c = 7.62068(2)$ Å	Mn	$-0.0041(19)$	0.2475(5)	0.2483(3)	0.22(1)
$V = 234.420(2)$ Å^3	O1	$-0.033(4)$	0.286(3)	0	0.18(15)
$R_p(\%) = 3.9$	O2$_1$	0.744(2)	0.019(2)	0.7833(9)	0.23(13)
$R_{wp}(\%) = 5.7$	O2$_2$	0.244(2)	0.519(2)	0.7526(9)	0.40(13)
$R_{Bragg}(\%) = 1.2$	O3	$-0.012(5)$	0.248(4)	$\frac{1}{2}$	0.30(16)
$\chi^2 = 3.9$					

Irreps, the uncertainty overcomes the value of the individual amplitudes so we set them to zero in our last refinement. The main difference between both models concerns the amplitude of the modes belonging to the Irrep GM5−, a bit higher in our refinement. This could be related to the differences between both experimental techniques as Yamada *et al.* [23] performed a single-crystal study refining anisotropic temperature factors for all atoms. In any case, the condensed modes are alike in both models and none of them are compatible with a Jahn-Teller deformation as seen previously in the study of PrBaMn$_2$O$_6$. Therefore, we discard the occurrence of a ferroic OO in any of the two samples.

TABLE IV. Summary of the mode decomposition with respect to its $P4/mmm$ parent structure of the $P2_1am$ structure of NdBaMn$_2$O$_6$ reported in this work and in Ref. [23].

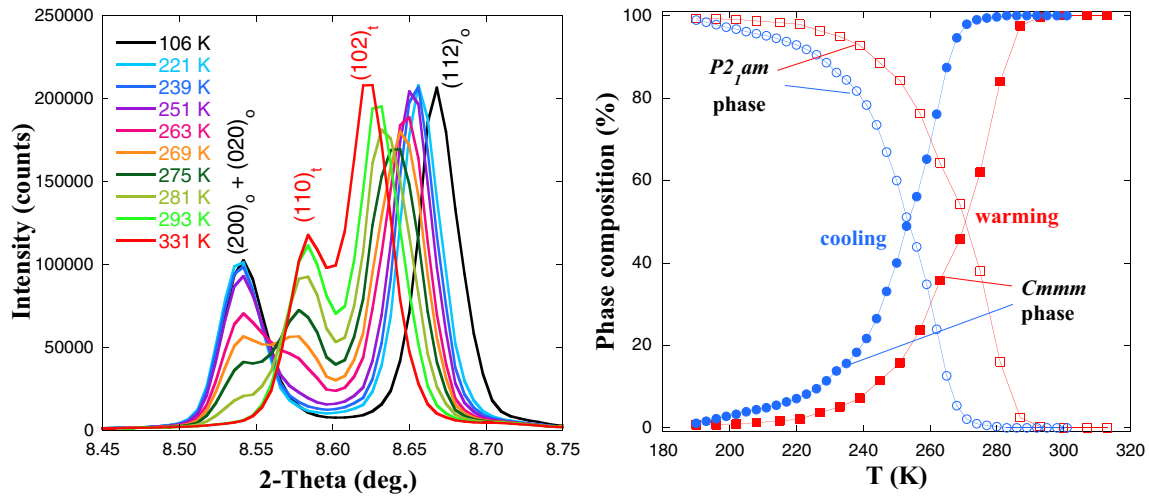|				Amplitude (Å)	
K vector	Irrep	Direction	Dim.	This work	Yamada *et al.* [23]
$(0, 0, 0)$	GM1+	(a)	2	0.07(1)	0.02(1)
$(0, 0, 0)$	GM5−	(a, a)	7	0.41(3)	0.21(1)
$(\frac{1}{2}, \frac{1}{2}, 0)$	M2+	(a)	1	0.00(7)	0.03(8)
$(\frac{1}{2}, \frac{1}{2}, 0)$	M3+	(a)	1	0.00(9)	0.03(5)
$(\frac{1}{2}, \frac{1}{2}, 0)$	M5−	$(a,0)$	6	0.44(2)	0.43(1)

FIG. 7. (left) Comparison of SXRPD patterns measured at the indicated temperatures heating from 100 K for NdBaMn$_2$O$_6$. Subscripts in the index refer to orthorhombic (o) and tetragonal (t) cells. (Right) Quantification of the high (closed symbols) and low (open symbols) temperature orthorhombic phases obtained from Rietveld analysis of SXRPD patterns in the heating (red squares) and cooling ramps (blue circles).

Unlike what happened in the PrBaMn$_2$O$_6$ sample, not all superstructure $(\frac{h}{2}, \frac{k}{2}, l)_t$ peaks disappear at T_N for NdBaMn$_2$O$_6$. In particular, the $(\frac{1}{2}, \frac{1}{2}, 0)_t$ peak is clearly noticeable in the pattern collected at 320 K (see Fig. S6 in the Supplemental Material [31]). Most of the other superstructure peaks have vanished in the pattern discarding the prevalence of the $P2_1am$ cell above T_N, but the NdBaMn$_2$O$_6$ cell is also not tetragonal at this temperature. The occurrence of this superstructure peak is accompanied by the broadening of $(h, 0, 0)_t$ peaks as can be seen in Fig. S6(b) [31]. These results agree with the finding of an orthorhombic unit cell with SG *Cmmm* in a previous study on a single crystal of NdBaMn$_2$O$_6$ [23]. The a and b axes in the *Cmmm* cell are twice those corresponding to the tetragonal cell. The superstructure peak is hardly noticeable in the patterns collected with normal statistics so it is difficult to settle down the transition temperature for the *Cmmm* $\rightarrow$ *P4/mmm* phase transition. For this purpose, DSC measurements (see Fig. S8 in Ref. [31]) have been carried out and a large peak has been observed at 289 K in the heating run at a speed of 20 K/min (279 K in the cooling one). This peak coincides with the structural transition coupled to the electrical and magnetic ones. The hysteresis agrees with a first-order transition. Hidden by this big anomaly, we have found a small and rounded anomaly centered at around 340 K in the cooling run. We think this is the signal of the *Cmmm* $\rightarrow$ *P4/mmm* phase transition. According to the symmetry analysis performed by ISODISTORT, this transition is expected to be continuous. The transition from *P4/mmm* to *Cmmm* involves nine active modes that are distributed in three Irreps: GM1+ (with two modes), GM2+ (one), and M5− (six). The M5− modes acting on the oxygen atoms implies a rotation around the b axis compatible with the one-tilt schema $a^0b^-c^0$. Therefore, the driving force for this transition is the strain produced by the small size of Nd^{3+} cations that is relieved by cooperative tilts of the MnO$_6$ octahedra. Refined structural parameters at 320 and 295 K can be found in Table III and the resulting calculated patterns of the SXRPD Rietveld profiles are displayed in Fig. S5 [31]. At lower tem-

peratures, this type of tilt is not enough and competes with the three-tilt system $a^-a^-c^+$ adopting the same cell of the PrBaMn$_2$O$_6$ compound with SG $P2_1am$. The latter SG is not a subgroup of *Cmmm* so the transition should be of first order. This transition shows a noticeable hysteresis (see Fig. 7). As in the Pr-based sample, the contribution of the high-temperature phase gradually decreases as the sample cools and becomes a diffuse contribution close to the peaks of the low-temperature phase, so the high-temperature phase remains on a nanoscopic scale at low temperature, but its quantification is difficult below 180–200 K. The hysteresis is a bit smaller than that observed in the Pr-based sample (compare Figs. 4 and 7). Another difference between both compositions is related to the number of transitions and the evolution of the lattice parameters due to the *P4/mmm* $\rightarrow$ *Cmmm* phase transition. Figure 8 shows the evolution of structural parameters as a function of the temperature. As can be seen in Fig. 8, the changes in the lattice parameters between the *P4/mmm* and *Cmmm* phases are very tiny and is it very hard to determine the transition point from SXRPD patterns and the highlighted regions should be taken as a rough approximation. On the other hand, the transition between *Cmmm* and $P2_1am$ is very noticeable and resembles that which occurred in the Pr-based sample between the *P4/mmm* and $P2_1am$ phases. There is a strong expansion of the a and b axes accompanied by a strong contraction of the c axis. This anisotropic behavior is accompanied by an increase in the volume of the unit cell, which would be in agreement with the electronic localization shown by the transport measurements. Regarding $\langle$Mn-O$\rangle$ and $\langle$Mn-O-Mn$\rangle$, there are also similarities with the Pr-based compound although the changes occur in two steps due to the existence of the *Cmmm* phase as can be seen in Fig. 8(d). The $\langle$Mn-O$\rangle$ distance slightly increases at the two phase transitions whereas the average bond angle significantly decreases. Given the similarity between NdBaMn$_2$O$_6$ and PrBaMn$_2$O$_6$, the electronic localization is also coupled to the asymmetric stretching distortion of the MnO$_6$ octahedra with two long and two short Mn-O2 distances as indicated in the Fig. 3(b).
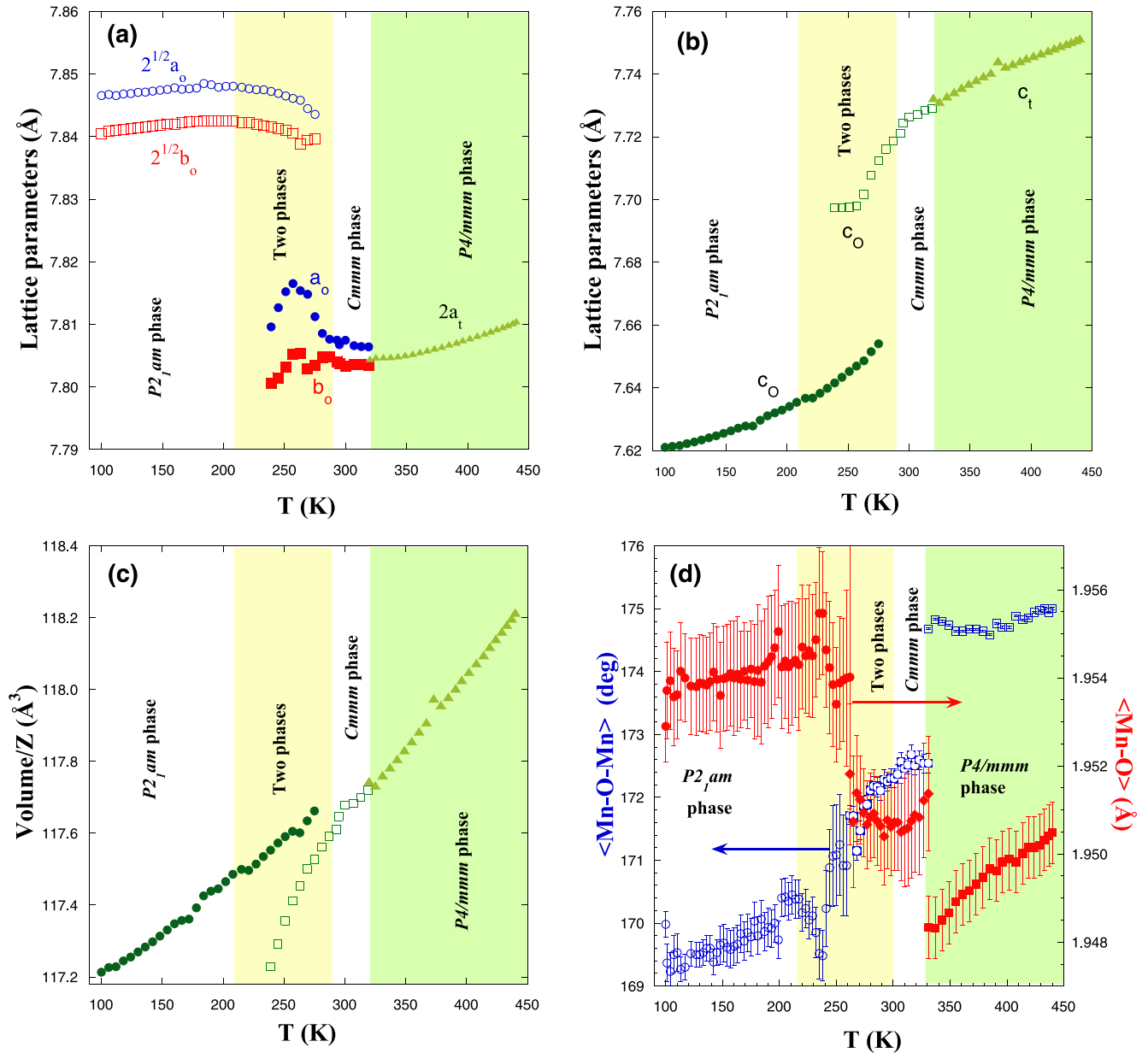
FIG. 8. Temperature dependence of the lattice parameters for $NdBaMn_2O_6$ in the heating ramp: (a) **a** and **b** axes, (b) **c** axis, and (c) unit cell volume. The lattice parameters of the **ab** plane have been multiplied by 2 ($P4/mmm$ phase) and $\sqrt{2}$ ($P2_1am$ phase) for the sake of comparison. (d) Temperature dependence of the average Mn-O-Mn bond angle (open symbols) and Mn-O distance (dark symbols) in the cooling ramp.

D. Raman spectroscopy

To elucidate the possible presence of a symmetry center in the low-temperature phases of $NdBaMn_2O_6$ and $PrBaMn_2O_6$, we have performed variable-temperature Raman measurements in the single-crystalline samples grown by the FZ technique. Not many studies have been made for $PrBaMn_2O_6$ and reports [24] for $NdBaMn_2O_6$ are not conclusive in this respect.

In a first experiment, spectra were recorded using the green 514.5 or 496.5 nm lines of an Ar^+ laser as excitation source, but the spectral intensity was weak because of strong absorption at those wavelengths; missing the observation of modes at low temperatures was suspected. Looking at the optical absorption spectrum [24] of $NdBaMn_2O_6$, we opted to excite at the minimum of the absorption curve using the 647.1 nm line of a Kr^+ laser. This procedure unveiled weak bands that remained obscured when exciting at higher energies.

FZ processed $RBaMn_2O_6$ double perovskites cleave easily along the $(001)_t$ plane, the growth direction being parallel to a $[110]_t$-like axis. Within such plane Raman spectra were measured in "parallel" and "crossed" configurations where "parallel" and "crossed" here mean along and perpendicular to the growth direction, respectively. Using the standard Porto's notation these spectra will be denoted as *xx* and *xy*. Allowing for the 45 ° rotation of the orthorhombic axes with respect to the tetragonal ones, the *x*, *y* directions so defined turn out to be coincident with the *x*, *y* axes of the low-temperature
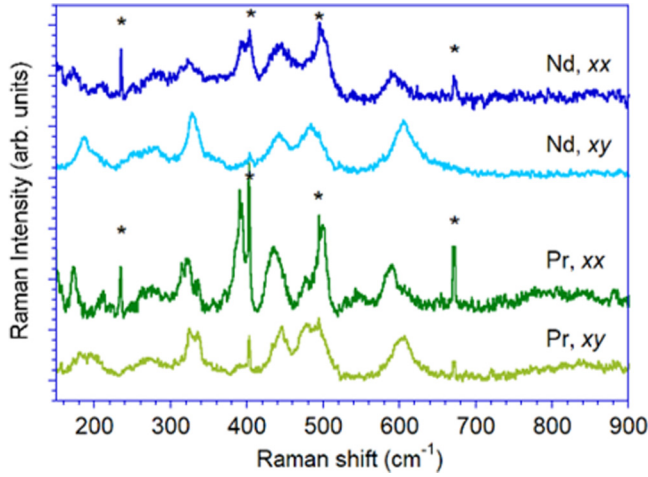
FIG. 9. Raman spectra of NdBaMn$_2$O$_6$ (at 150 K) and PrBaMn$_2$O$_6$ (at 77 K) in *xx* and *xy* configurations recorded with $\lambda = 647.1$ nm. Peaks arising from laser plasma lines are marked with an asterisk.

orthorhombic phase, so that the cleavage plane is identified as (001)$_o$.

Figure 9 shows low *T* spectra of NdBaMn$_2$O$_6$ and PrBaMn$_2$O$_6$ in *xx* and *xy* configurations. Raman spectra were analyzed according to the Raman activity expected for the possible low-temperature phases and taking into account the experiment geometry. According to the site occupancies listed in Tables II and III, 57 Raman active modes are predicted in the noncentrosymmetric $P2_1am$ phase ($16A_1 + 13A_2 + 12B_1 + 16B_2$), but only the A_1 and A_2 modes are accessi-

ble for polarization within the (001)$_o$ plane. We therefore expect to see 29 modes, 16 A_1 in parallel and 13 A_2 in crossed configurations. If the structure was centrosymmetric with *Pmam* SG, 30 Raman active modes would be expected ($8A_g + 5B_{1g} + 7B_{2g} + 10B_{3g}$) but only 13 would be observable in the explored configuration ($8A_g$ in parallel and $5B_{1g}$ in crossed polarization).

Spectra were decomposed as a superposition of pseudo-Voigt profiles and the obtained wave numbers are listed in Table V. We thus find ~ten modes in *xx* and ~nine modes in *xy* for NdBaMn$_2$O$_6$ at 150 K. For PrBaMn$_2$O$_6$ ~ 17 modes are found in *xx* and ~13 in *xy* configurations at 77 K (some identifications are uncertain because of the low intensity). These numbers exceed the expectations for the *Pmam* SG and agree better with the predictions of the $P2_1am$ SG. Raman measurements therefore support that the low-temperature phase of both compounds is noncentrosymmetric. In this respect, we note that in the Raman study of NdBaMn$_2$O$_6$ by Mero *et al.* [24] with the laser at 532 nm, only eight modes were detected at 20 K for measurements also restricted to the (001)$_o$ plane, which is compatible with both the centrosymmetric and the noncentrosymmetric structures. The discrepancy with our study may be a consequence of their using an excitation wavelength in coincidence with a strong absorption band.

Spectra at room temperature can be interpreted within a tetragonal symmetry for both compounds, yielding six Raman active modes ($2A_{1g} + B_{1g} + 3E_g$) but only $2A_{1g} + B_{1g}$ are accessible in the (001)$_t$ plane and identified at ~278 and 479 cm^{-1} (A_{1g}) and 326 cm^{-1} (B_{1g}). Although NdBaMn$_2$O$_6$ is actually orthorhombic at room temperature, with *Cmmm* SG and 30 expected Raman active modes, a quasitetragonal

TABLE V. Raman wavenumbers (cm^{-1}) below 700 cm^{-1} observed in NdBaMn$_2$O$_6$ and PrBaMn$_2$O$_6$ at low temperature in *xx* (//) and *xy* (*X*) configurations, where *x* and *y* stand for the principal axes of the low-temperature orthorhombic phase.

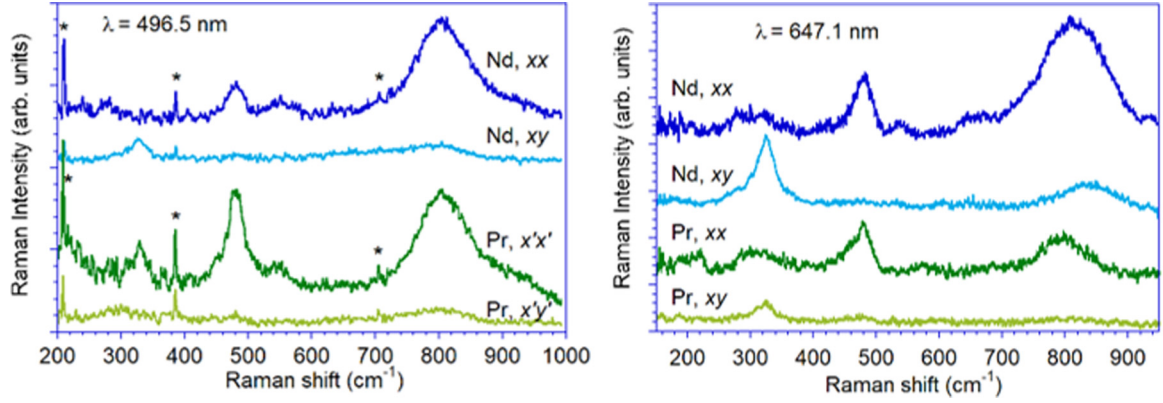| NdBaMn$_2$O$_6$				PrBaMn$_2$O$_6$			
77 //	77 *X*	150//	150 *X*	77 //	77 *X*	150 //	150 *X*
152		150		148	153	147	153
170		171		172	179	172	174
	191		185		199	180	195
210	208	207	197	210		209	
					243	224	244
268	255	248.5	254	261	270	267	274
	281	281	279	276		291	307
				315	325	315	
327	329	323.5	329	323	327	324	323
				335	335	333	335
				356		358	336
				370		371	
391		393		390	393	392	393
430				435	444	440	442
438	438	442	442	480	474	476	474
474	476			499	493	497	493
500	491	499	485	545		537	
						559	
583	599	592	604	587		588	
601				599	603		605

FIG. 10. Left: Room temperature Raman spectra of $NdBaMn_2O_6$ and $PrBaMn_2O_6$ recorded with $\lambda = 496.5$ nm. Right: Same but with $\lambda = 647.1$ nm. Note that in the 496.5 nm spectra the $PrBaMn_2O_6$ axes (x', y') are rotated 45 ° with respect to those of $NdBaMn_2O_6$ (x, y). Asterisks denote laser plasma lines.

symmetry may be apparent because of either the small orthorhombic distortion or local heating induced by the laser, producing the transition to the $P4/mmm$ phase.

A most interesting feature of the Raman spectra of both compounds is the appearance of an intense and broad band around 800 cm^{-1} (Fig. 10). This Raman shift is much higher than vibrational wave numbers reported for $RBaMn_2O_6$ and other manganites [40], so a phononic origin may be discarded. As shown in Fig. 11 for $NdBaMn_2O_6$, the band is absent or very weak at 77 K and is enhanced above 220 K, in good coincidence with the melting of the AFM order and the appearance of short-range FM fluctuations prior to the Néel temperature [23], which suggests it may have a magnetic origin. In fact, the growth of this band coincides with the temperature region where the high- and low-temperature phases coexist (see Fig. 7) and the first one has short-range FM correlations [25]. The detection of the band upon excitation at different wavelengths confirms that the band is of Raman type and not due to emission. Its polarization properties indicate that it has mainly A_1 or A_{1g} character, although a non-negligible intensity is observed for $NdBaMn_2O_6$ in the xy channel (B_{1g} quasite-

tragonal symmetry) at room temperature. The high intensity of the band in the PM phase suggests that it may arise from short-range magnetic interactions still present in that phase and its mainly A_1 or A_{1g} symmetry points to a second-order excitation.

IV. CONCLUSIONS

We have studied the structural properties of $RBaMn_2O_6$ ($R = $ La, Pr, and Nd) using SXRPD and Raman spectroscopy as a function of temperature. The three samples are isostructural at high temperature (440 K) adopting the tetragonal structure of a perovskite with A-site ordering without tilts of the MnO_6 octahedron (SG $P4/mmm$). $LaBaMn_2O_6$ undergoes a ferromagnetic phase transition with anisotropic changes in the lattice parameters related to the orientation of the Mn ordered moments. The unit cell symmetry remains tetragonal down to 150 K.

$PrBaMn_2O_6$ has two consecutive magnetic transitions following the sequence PM→FM→AFM when cooling down. At T_C, the tetragonal cell experiences the same changes as seen in $LaBaMn_2O_6$ indicating a similar FM order. At T_N, a structural phase transition coupled to an electronic localization is observed. The low-temperature phase is orthorhombic with lattice vectors (1, 1, 0), (−1, 1, 0), and (0, 0, 1) with respect to the high-temperature tetragonal phase. The transition exhibits a large hysteresis with a coexistence of the two phases in a wide temperature range. The presence of diffuse scattering in the diagrams measured at low temperature replacing the diffraction peaks of the high-temperature phase indicates that nanoscopic regions of the tetragonal phase still persist at 100 K. There are two possible structures capable of accounting for the diffraction patterns but the active modes identified by the Raman spectroscopy clearly determine that the SG of the low-temperature phase is the noncentrosymmetric $P2_1am$. The symmetry analysis identified the driving modes for the phase transition that belong to the Irreps M5− (associated with MnO_6 rotation) and GM5− (related to asymmetric stretching and scissoring modes). No stretching modes associated with a Jahn-Teller distortion are identified in this transition.
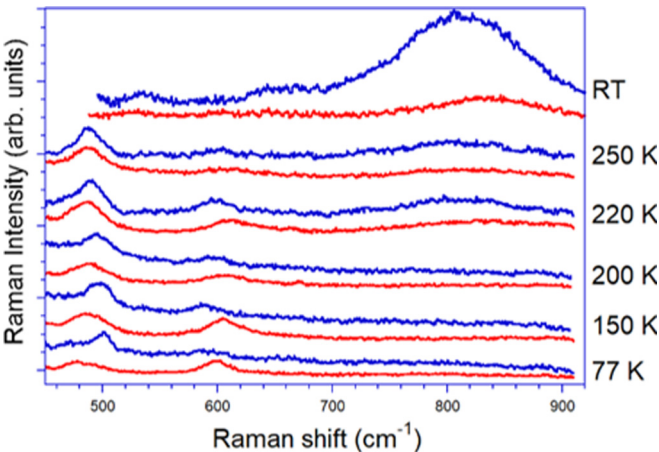

FIG. 11. Temperature dependence of the Raman spectra of $NdBaMn_2O_6$ in the 450–900 cm^{-1} region. Blue (red) spectra correspond to measurements in xx (xy) configurations. $\lambda = 647.1$ nm.

NdBaMn$_2$O$_6$ has macroscopic properties similar to PrBaMn$_2$O$_6$. However, the temperature dependence of the lattice parameters does not reveal the anisotropic changes observed at T_C in both PrBaMn$_2$O$_6$ and LaBaMn$_2$O$_6$. This is in accordance with the lack of long-range FM order reported for this sample [25]. In this way, NdBaMn$_2$O$_6$ exhibits second-order Raman scattering features above 220 K that reflect short-range FM correlations. NdBaMn$_2$O$_6$ undergoes a structural phase transition in the PM region due to cooperative tilts of MnO$_6$ octahedra at around 340 K. On cooling, it displays a first-order transition coupled to a metal-insulator-like transition with similar hysteresis and coexistence of phases to those observed in PrBaMn$_2$O$_6$. SXRPD patterns reveal that NdBaMn$_2$O$_6$ and PrBaMn$_2$O$_6$ are isostructural at 100 K adopting the same distorted structure with SG $P2_1am$. This is a polar structure where spontaneous polarization in the a axis direction is expected and the main contribution comes from the shift of the oxygen atoms. Unfortunately, accurate measurements of $P(E)$ loops at low temperature in our samples were not possible due to the strong contribution of leakage currents. Furthermore, there is a single nonequivalent site for the Mn atom in the $P2_1am$ cell, incompatible with the occurrence of a CO phase. Therefore, we discard that NdBaMn$_2$O$_6$ is isostructural to SmBaMn$_2$O$_6$ and in fact we have not found the $(\frac{h}{4}, \frac{k}{4}, l)_t$ superstructure peaks characteristic of the low-temperature phase of SmBaMn$_2$O$_6$ [18,25]. As a concluding remark, the practically zero value of the stretching mode associated with a Jahn-Teller distortion in the formation of the $P2_1am$ cell suggests that the existence of a ferroic OO of e_g ($3d_{x^2-y^2}$) orbitals in PrBaMn$_2$O$_6$ and NdBaMn$_2$O$_6$ is very unlikely. Instead, the electronic localization in PrBaMn$_2$O$_6$ and NdBaMn$_2$O$_6$ has a structural origin and it is mostly driven by a decrease of the ⟨Mn-O-Mn⟩ bond angle that narrows the electronic band width and stabilizes a periodic distorted state alternating long and short Mn-O bonds in the ab plane.

[1] Y. Tokura, Rep. Prog. Phys. **69**, 797 (2006).

[2] E. Dagotto, T. Hotta, and A. Moreo, Phys. Rep. **344**, 1 (2001).

[3] J. M. D. Coey, M. Viret, and S. Molnar, Adv. Phys. **48**, 167 (1999).

[4] Y. Tokura and N. Nagaosa, Science **288**, 462 (2000).

[5] Y. Ueda and T. Nakajima, Prog. Solid State Chem. **35**, 397 (2007).

[6] R. Kajimoto, H. Yoshizawa, H. Kawano, H. Kuwahara, Y. Tokura, K. Ohoyama, and M. Ohashi, Phys Rev. B **60**, 9506 (1999).

[7] J. Geck, D. Bruns, C. Hess, R. Klingeler, M. v. Zimmermann, S.-W. Cheong, and B. Büchner, Phys. Rev. B **66**, 184407 (2002).

[8] Y. Tomioka, A. Asamitsu, Y. Moritomo, H. Kuwahara, and Y. Tokura, Phys. Rev. Lett. **74**, 5108 (1995).

[9] Z. Jirác, S. Krupika, Z. Simsa, M. Dlouhá, and S. Vratislav, J. Magn. Magn. Mater. **53**, 153 (1985).

[10] P. G. Radaelli, D. E. Cox, M. Marezio, S.-W. Cheong, P. E. Schiffer, and A. P. Ramirez, Phys Rev. Lett. **75**, 4488 (1995).

[11] R. J. Goff and J. P. Attfield, Phys. Rev. B **70**, 140404(R) (2004).

[12] J. Herrero-Martin, J. García, G. Subías, J. Blasco, and M. Concepción Sánchez. Phys. Rev. B **70**, 024408 (2004).

[13] S. Lafuerza, J. García, G. Subías, J. Blasco, and P. Glatzel, Phys. Rev. B **93**, 205108 (2016).

[14] R. Maezono, S. Ishihara, and N. Nagaosa, Phys. Rev. B **57**, R13993 (1998).

[15] H. Kuwahara, T. Okuda, Y. Tomioka, A. Asamitsu, and Y. Tokura, Phys. Rev. Lett. **82**, 4316 (1999).

[16] T. Nakajima, H. Kageyama, H. Yoshizawa, and Y. Ueda, J. Phys. Soc. Jpn. **71**, 2843 (2002).

[17] A. J. Williams and J. P. Attfield, Phys. Rev. B **72**, 024436 (2005).

[18] D. Morikawa, K. Tsuda, Y. Maeda, S. Yamada, and T. Arima, J. Phys. Soc. Jpn. **81**, 093602 (2012).

[19] M. García-Fernández, U. Staub, Y. Bodenthin, S. M. Lawrence, A. M. Mulders, C. E. Buckley, S. Weyeneth, E. Pomjakushina, and K. Conder, Phys. Rev. B **77**, 060402(R) (2008).

[20] E. A. Nowadnick, J. He, and C. J. Fennie, Phys. Rev. B **100**, 195129 (2019).

[21] F. Millange, V. Caignaert, B. Domengès, B. Raveau, and E. Suard, Chem. Mater. **10**, 1974 (1998).

[22] T. Nakajima, H. Kageyama, H. Yoshizawa, K. Ohoyama, and Y. Ueda, J. Phys. Soc. Jpn. **72**, 3237 (2003).

[23] S. Yamada, H. Sagayama, K. Higuchi, T. Sasaki, K. Sugimoto, and T. Arima, Phys. Rev. B **95**, 035101 (2017).

[24] R. D. Mero, K. Ogawa, S. Yamada, and H.-L. Liu, Sci. Rep. **9**, 18164 (2019).

[25] D. Akahoshi, Y. Okimoto, M. Kubota, R. Kumai, T. Arima, Y. Tomioka, and Y. Tokura, Phys. Rev. B **70**, 064418 (2004).

[26] S. Yamada, N. Abe, H. Sagayama, K. Ogawa, T. Yamagami, and T. Arima, Phys. Rev. Lett. **123**, 126602 (2019).

[27] S. V. Trukhanov, L. S. Lobanovski, M. V. Bushinsky, V. V. Fedotova, I. O. Troyanchuk, A. V. Trukhanov, V. A. Ryzhov, H. Szymczak, R. Szymczak, and M. Baran, J. Phys.: Condens. Matter **17**, 6495 (2005).

[28] J. Blasco, M. C. Sánchez, J. García, J. Stankiewicz, and J. Herrero-Martín, J. Cryst. Growth **310**, 3247 (2008).

[29] J. Rodríguez-Carvajal, Phys. B (Amsterdam, Neth.) **192**, 55 (1992).

[30] F. Fauth, I. Peral, C. Popescu, and M. Knapp, Powder Diffr. **28**, S360 (2013).

[31] See Supplemental Material at http://link.aps.org/supplemental/10.1103/PhysRevB.103.064105 for details about x-ray diffraction refinements of LaBaMn$_2$O$_6$, PrBaMn$_2$O$_6$, and

$NdBaMn_2O_6$; comparison of the SRXRD patterns taken at 100 and 400 K for $PrBaMn_2O_6$ and $NdBaMn_2O_6$; temperature dependence of details of the SRXRD patterns for Pr- and Nd-based samples and DSC measurements of $NdBaMn_2O_6$.

[32] H. T. Stokes, D. M. Hatch, and J. D. Wells, Phys. Rev. B **43**, 11010 (1991).

[33] C. J. Howard and H. T. Stokes, Acta Crystallogr., Sect. B **60**, 674 (2004).

[34] A. M. Glazer, Acta Crystallogr., Sect. A **31**, 756 (1975).

[35] C. Autret, A. Maignan, C. Martin, M. Hervieu, V. Hardy, S. Hébert, and B. Raveau, Appl. Phys. Lett. **82**, 4746 (2003).

[36] J. B. Goodenough, Aust. J. Phys. **52**, 155 (1999).

[37] S. Johnston, A. Mukherjee, I. Elfimov, M. Berciu, and G. A. Sawatzky, Phys. Rev. Lett. **112**, 106404 (2014).

[38] We have studied the $SmBaMn_2O_6$ compound and the intensity of noticeable $(\frac{h}{4}, \frac{k}{4}, 1)_t$ superstructure peaks range between 5.5×10^{-5} and 3.3×10^{-3} of the main diffraction peak (manuscript in preparation).

[39] J. M. Pérez-Mato, D. Orobengoa, and M. I. Aroyo, Acta Crystallogr., Sect. A **66**, 558 (2010).

[40] V. B. Podobedov and A. Weber, Raman scattering in perovskite manganites, in *Raman Scattering in Materials Science*, edited by W. H. Weber and R. Merlin, Springer Series in Materials Science (Springer, Berlin, Heidelberg, 2000), Vol. 42.